



Contents lists available at ScienceDirect

Arabian Journal of Chemistry

journal homepage: [www.sciencedirect.com](http://www.sciencedirect.com)

Original article

# Synthesis of Ruthenium (II) trisbipyridine complex containing ionic liquids immobilized on fibrous $\text{CoMn}_2\text{O}_4$ for isolation of asphaltene from petroleum

Xinlin He <sup>a,\*</sup>, Rahele Zhiani <sup>b,\*</sup><sup>a</sup> Xijing University, Xi'an 710123, China<sup>b</sup> New Materials Technology and Processing Research Center, Department of Chemistry, Neyshabur Branch, Islamic Azad University, Neyshabur, Iran

## ARTICLE INFO

## Article history:

Received 29 April 2023

Accepted 20 September 2023

Available online 26 September 2023

## Keywords:

Nanoadsorbent  
Green chemistry  
 $\text{CoMn}_2\text{O}_4$   
Asphaltene  
Crude oil

## ABSTRACT

The formation of a durable nanoadsorbent, known as  $\text{DFCoMn}_2\text{O}_4/\text{IL@Ru(II)}$ , was achieved by binding a complex of Ru (II) trisbipyridine with ionic liquids (IL) to a dendritic fibrous  $\text{CoMn}_2\text{O}_4$  ( $\text{DFCoMn}_2\text{O}_4$ ). The resulting  $\text{DFCoMn}_2\text{O}_4/\text{IL@Ru(II)}$  was characterized using various techniques such as X-ray diffraction analysis (XRD), fourier-transform infrared spectroscopy (FTIR), atomic force microscopy (AFM), thermal gravimetric analysis (TGA), transmission electron microscopy (TEM), vibrating sample magnetometer (VSM), and scanning electron microscopy (SEM).  $\text{DFCoMn}_2\text{O}_4/\text{IL@Ru(II)}$  was then employed as an environmentally friendly adsorbent for the removal and adsorption of asphaltene from petroleum. The presence of fibrous  $\text{CoMn}_2\text{O}_4$  categories enhanced the adsorption capacity and facilitated the recovery of the adsorbent without significantly reducing the efficiency. The results demonstrated a clear synergistic effect between dendritic fibrous  $\text{CoMn}_2\text{O}_4$  and the  $\text{IL@Ru(II)}$  categories, exhibiting a strong correlation. The utilization of the  $\text{DFCoMn}_2\text{O}_4/\text{IL@Ru(II)}$  system resulted in quasi-second-order adsorption kinetics. The experiment was conducted using the Taguchi method to minimize costs and time. Various amounts of asphaltene, temperatures, and adsorbent quantities were examined. Minitab software was deployed to evaluate the impact of these variables on asphaltene adsorption. The presence of ionic liquid groups enhanced the solubility of the heterogeneous adsorbent in environmentally friendly solvents, thereby enhancing function and reducing the time.

© 2023 The Author(s). Published by Elsevier B.V. on behalf of King Saud University. This is an open access article under the CC BY license (<http://creativecommons.org/licenses/by/4.0/>).

## 1. Introduction

Precipitation of heavy hydrocarbon substances contains two categories of wax and asphaltene. The formation of sediments causes the closing of process and wells transfer lines, the breakdown of process equipment, and a drastic reduction of catalyst efficiency. Facing the issue of asphaltene precipitation in upstream industries, two methods have been used to hinder deposit generation and descaling treatment. In the procedure adjustment approach, besides thermodynamic equilibrium situations, the fluid

retention duration is an influencing element in causing sedimentation. External force employment, chemical treatment, heat treatment, biotechnology, and mechanical operation are some techniques of asphaltene elimination in the generation and exploitation procedures (Liu et al., 2010; Pikul et al., 2013). There are four approaches to eliminating asphaltene from petroleum of namely, supercritical extraction, asphalt emulsion, solvent asphalt, and asphalt oxidation (Huang et al., 2016; Zhu et al., 2015; Bai et al., 2014).

A variety of elements influence the generation and precipitation of heavy organic substances from petroleum, such as the features, percentage composition of petroleum, the sort of injected fluid, temperature, pressure, and traits of canals through which the tank fluid flows (Medina et al., 2023; Wang et al., 2023; Alalwani et al., 2023; Arias-Madrid et al., 2020). Failure to remove asphaltene from crude oil leads to irrecoverable losses to the petrochemical industry. Therefore, many techniques have been presented to eliminate asphaltene (Medina et al., 2020; Medina et al., 2021; Medina et al., 2019).

\* Corresponding authors.

E-mail addresses: [hexinlinhz@163.com](mailto:hexinlinhz@163.com) (X. He), [R\\_zhiani2006@yahoo.com](mailto:R_zhiani2006@yahoo.com), [R\\_zhiani2006@iau-neyshabur.ac.ir](mailto:R_zhiani2006@iau-neyshabur.ac.ir) (R. Zhiani).

Peer review under responsibility of King Saud University.



Production and hosting by Elsevier

<https://doi.org/10.1016/j.arabjc.2023.105289>1878-5352/© 2023 The Author(s). Published by Elsevier B.V. on behalf of King Saud University. This is an open access article under the CC BY license (<http://creativecommons.org/licenses/by/4.0/>).

The quantity of adsorbed asphaltene on NPs is highly dependent on the sort of exterior level chemistry of the nanoparticles and the interaction force between asphaltene and nanoparticles (Medina et al., 2021). Forces for asphaltene adsorption on NPs principally comprise the level load of asphaltene, and the base-acid interplay between the exterior level of asphaltene and NPs (Zhao et al., 2023).

Lately, organoruthenium half-sandwich metal complex has been broadly investigated considering their pharmacological and catalytic traits (Khan and Süss-Fink, 2012). Catalytic potential, their reactivity, and biological performance may be adjusted by employing an appropriate selection of ligands. The support of Ru complexes on catalytic structure such as dendrimers, liposomes, metals, and other metal nanostructures was done with the aim of preventing agglomeration (Wu et al., 2011). Furthermore, such progress opens up opportunities in this field such as the development of molecular nanomagnetism as well as the preparation of single-molecule magnets (Rosado Piquer et al., 2017; Holmberg et al., 2013).

Gold (Au), platinum (Pt), palladium (Pd), and silver (Ag) are examples of precious metal catalysts that have demonstrated superior performance in comparison to transition metal oxides such as cobalt oxide (CoO) and manganese oxide (MnO) (Steele and Heinzl, 2001; Meng et al., 2007; Liu et al., 2011; Cao et al., 2003; Salehi et al., 2016; Yang et al., 2016; Yao et al., 2016; Fujiwara et al., 2016; Zhiani et al., 2018; Sadeghzadeh, 2016). However, precious metal catalysts are susceptible to issues such as easy poisoning and limited availability, which makes them expensive to obtain. Consequently, there is a need to develop transition metal oxide catalysts that are cost-effective and possess high thermal stability, as alternatives to noble metal catalysts (Hassankhani et al., 2018; Salehi et al., 2016; Zinatloo-Ajabshir et al., 2016; Wang et al., 2013). In the group of the transition metals, manganese (Mn), cobalt (Co), and their respective oxides have been identified as praising catalysts due to their satisfactory performance at low temperatures and affordable prices. Notably, the following order of catalytic activity was observed in the oxidation of benzene and toluene:  $Mn_2O_3 > Mn_3O_4 > MnO_2$ . Additionally, the catalytic function was further enhanced by the introduction of alkali and alkaline earth metals (Bezerra Lopes et al., 2009; Besikiotis et al., 2012; Wang et al., 2012; Sanchez-Bautista et al., 2010).

Here, dendritic fibrous  $CoMn_2O_4$  nanoparticles were employed to adsorb and eliminate asphaltene from oil. First, dendritic fibrous  $CoMn_2O_4$  nanoparticles were activated by trisbipyridine complex. Ruthenium (II) categories containing ionic liquids were then immobilized on  $CoMn_2O_4$  fibers, and  $DFCoMn_2O_4/IL@Ru(II)$  nanoparticle was employed as a reusable and robust adsorbent to remove asphaltene.

## 2. Experimental

### 2.1. Materials and methods

Chemical materials were procured from Fluka and Merck with a high degree of purity. The determination of melting points was conducted in open capillaries utilizing an Electrothermal 9100 instrument, and the results obtained were not corrected. The observation of particle magnitude and structure of the nano particle was accomplished through the utilization of a Philips CM10 transmission electron microscope, operating at 100 kV. FE-SEM images were obtained using a HITACHI S-4160 instrument. XPS investigations were carried out employing an XR3E2 (VG Microtech) twin anode X-ray source, where the  $AlK\alpha$  energy was determined to be 1486.6 eV. Energy dispersive X-ray spectroscopy

(EDX) was conducted utilizing a field emission scanning electron microscope (FESEM, JEOL 7600F) with a spectrometer for the energy dispersion of X-rays sourced from Oxford instruments. Powder X-ray diffraction data were acquired using a Bruker D8 Advance model with Cu  $ka$  radiation. ICP experiments were conducted utilizing a VARIAN VISTA-PRO CCD simultaneous ICP-OES instrument. The NPs' exterior level, vent magnitude, and vent width were ascertained through  $N_2$  physisorption at a temperature of  $-196^\circ C$  employing an exterior level and vent magnitude analyzer, specifically the Micromeritics ASAP 2000 instrument, by employing the BET method. The products' purity specification and reaction tracking were executed by means of TLC on silica gel polygram SILG/UV 254 plates.

### 2.2. Manufacturing of fibrous $CoMn_2O_4$ NPs

1.9 mL of an aqueous solution containing  $Co(NO_3)_2 \cdot 6H_2O$  (at a concentration of 45 mL),  $Mn(NO_3)_2 \cdot 4H_2O$  (also at a concentration of 50 mL), 1-pentanol (at a volume of 20 mL), and cyclohexane (at a volume of 0.8 L) were mixed. Additionally, a stirred blend of cetylpyridinium bromide (weighing 650 mg) and 1.3 mL of an aqueous solution containing ascorbic acid (with a concentration of 0.08 M) were introduced. The resulting mixture was thoroughly mixed at a temperature of  $25^\circ C$  for a duration of 45 min, then transferred to a reactor and heated to a temperature of  $100^\circ C$  for a period of 7 h. Subsequently, the  $CoMn_2O_4$  fibrous nanoparticles were separated using a centrifuge and cleansed by immersion in a solution composed of water and acetone. Finally, the separated nanoparticles were dried in an oven.

### 2.3. Fabrication of ionic liquid

20 mmol of imidazole was released in tetrahydrofuran (THF) (20 mL) and NaH (26 mmol) was added via ultrasonication. Next, 3-bromopropyl trimethoxysilane (27 mmol) was released into the amalgam, and blended for 15.5 h at  $68^\circ C$ . 4.5 mmol of 1,3-dibromopropane and 2.0 mmol of 2,2'-bipyridinyl-4,4'-diol were added to the mixture and 15 h refluxed again. The outcome was filtered and eluted with water and methanol. The final product was vacuum-dried at  $70^\circ C$  for 1 h.

### 2.4. Fabrication of $DFCoMn_2O_4/IL$ NPs

200 mg  $DFCoMn_2O_4$ , 80 mL amalgam of ethanol, 20 mL deionized water, 32 wt% concentrated ammonia aqueous amalgam ( $NH_3 \cdot H_2O$ , 3.5 mL), and IL (35 mmol) were combined. The produced suspension was filtered after vigorous stirring and then dried at  $50^\circ C$  in the participation of air.

### 2.5. Fabrication of $DFCoMn_2O_4/IL@Ru(II)$ NPs

68 mg  $DFCoMn_2O_4/IL$  and 2.7 mg  $RuCl_3 \cdot 3H_2O$  were poured into a wet EtOH/DMF 2:8 (6 mL) amalgam and heated at  $90^\circ C$  for 72 h. The outcome was refrigerated at  $25^\circ C$  and vacuumed. The remnant was added to  $CH_2Cl_2$  and eluted with deionized water. A saturated amalgam of  $NH_4PF_6$  (9 mL) was released, the resulting solid was collected by an external magnet, and vacuum-dried.

### 2.6. Asphalt elimination

To investigate the elimination of asphaltene, specific quantities of adsorbents were introduced into a 10 mL standard solution of asphaltene dissolved in n-heptane (100–2500 mg/L). The resulting mixture underwent blending for a duration of 3 h at ambient temperature. The blend was then subjected to the removal of

$DFCoMn_2O_4/IL@Ru(II)$  NPs. Subsequently, the UV–Vis method was employed to measure the absorbance of the solutions.

### 3. Results and discussion

The  $DFCoMn_2O_4$  amalgam was synthesized through established methodologies and then subjected to functionalization using an IL. Subsequently, a reductive amination process was conducted to generate co-immobilized Ru(II) species (Scheme 1).

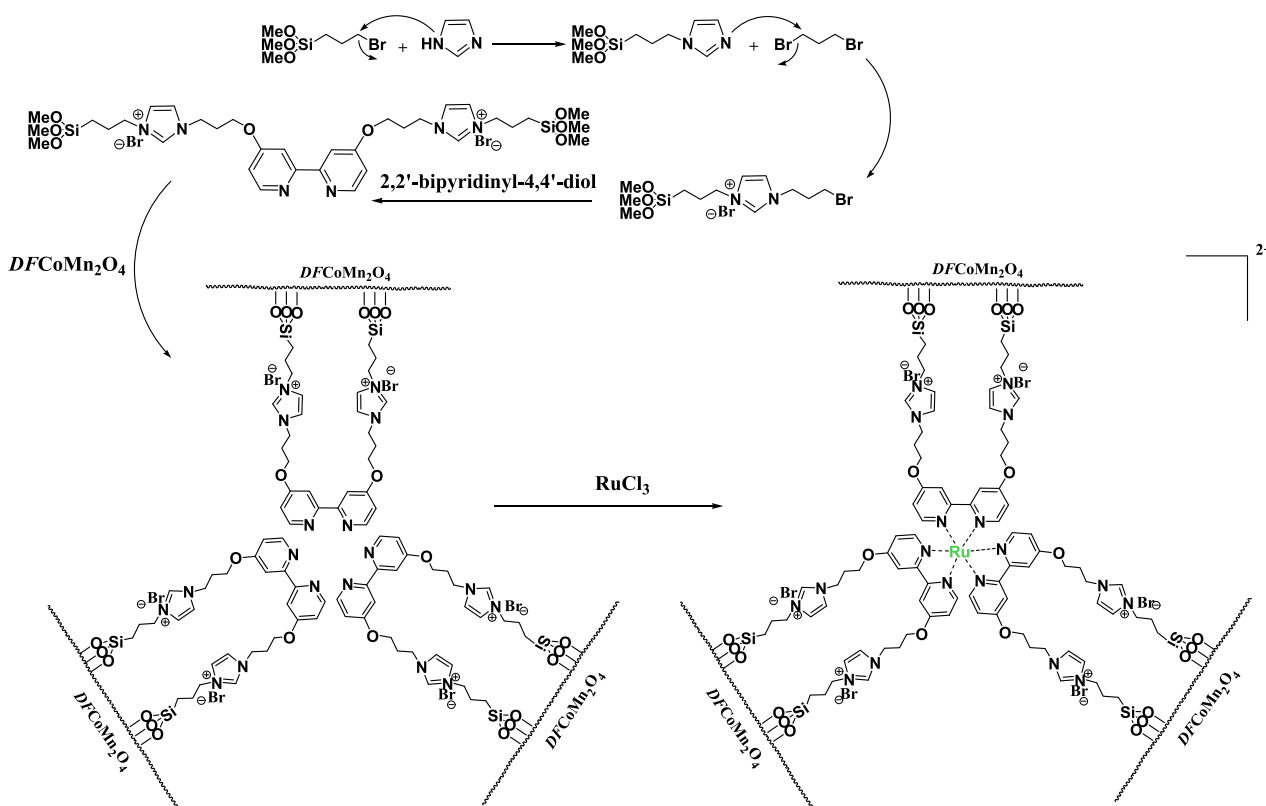
The scanning electron microscopy (SEM) and transmission electron microscopy (TEM) analyses were employed to investigate the anatomy and morphology of  $DFCoMn_2O_4/IL@Ru(II)$  (Fig. 1). As shown in Fig. 1a, the  $DFCoMn_2O_4/IL@Ru(II)$  exhibits a non-porous structure with  $CoMn_2O_4$  fibers. The specimens display spheres of equal magnitude of approximately 280 nm and possess a creased radial arrangement. Detailed examination of the FESEM and TEM patterns unveiled that the  $DFCoMn_2O_4/IL@Ru(II)$  comprises 3D dendrimeric fibers with a magnitude range of 9–12 nm, which constitute walls and offer direct entry to the uppermost external level.

Fig. 2 illustrates the TGA analysis of  $DFCoMn_2O_4/IL@Ru(II)$ . The decrease in mass of 29.1 wt% observed in the temperature range of 270–390 °C can be attributed to the removal of chemically and physically absorbed solvent present on the outer surface of the  $DFCoMn_2O_4/IL@Ru(II)$  NPs. This reduction in weight can be ascribed to the presence of organic groups. The decrease in weight at 270–390 °C can be explained by the oxidation of Ru(II). The remaining mass after the dissociation of IL@Ru(II) is the outcome of the diffusion of  $DFCoMn_2O_4$ . The X-ray diffraction (XRD) technique was utilized in order to investigate the nanostructured  $DFCoMn_2O_4/IL@Ru(II)$ . It was observed that all of the diffraction peaks displayed in Fig. 3 were in alignment with the pure fluorite  $DFCoMn_2O_4/IL@Ru(II)$  sample, indicating the absence of any impu-

rities (JCPDS no. 77–0471). Furthermore, Fig. 4 illustrates the use of the energy-dispersive X-ray spectroscopy (EDX) spectrum in ascertaining the existence of particular atoms within the fibrous composition of the  $DFCoMn_2O_4$  nanoparticles. The identification of N, Mn, Co, and O in the spectrum confirmed that the fabrication of the  $DFCoMn_2O_4$  sample was carried out accurately.

The FTIR spectra provided evidence of the involvement of N, O, Co, and organic surfaces in both the nanoparticles of  $DFCoMn_2O_4$  and the  $DFCoMn_2O_4/IL@Ru(II)$  composite. In the case of  $DFCoMn_2O_4$ , the broad absorption regions observed at 1084 and 3422  $cm^{-1}$  were attributed to Co–O asymmetric mapping and H–O, respectively. Similarly, the peaks observed at 799 and 461  $cm^{-1}$  were linked to Mn–O symmetrical expansion and flexure, respectively (Fig. 5a). The peaks observed in the spectra corresponded to the interaction between IL@Ru(II) and the outer layer of  $DFCoMn_2O_4$ . The composite material,  $DFCoMn_2O_4/IL@Ru(II)$ , exhibited prominent bands at approximately 1091, 793, and 462  $cm^{-1}$ . In the range of 3100–3560  $cm^{-1}$ , a strong and broad absorption band could be attributed to the elongation oscillations of –OH groups. Summits at 3430  $cm^{-1}$  and 2930  $cm^{-1}$  were indicative of the stretching vibrations of aromatic hydrogen-carbon bonds and aliphatic moieties, respectively (Fig. 5b).

The analysis of Nitrogen physisorption indicated that the specific BET area of  $DFCoMn_2O_4$  and  $DFCoMn_2O_4/IL@Ru(II)$  were approximately 709 and 386  $m^2/g$ , respectively. The reduction in the level of  $DFCoMn_2O_4/IL@Ru(II)$  (in comparison to  $DFCoMn_2O_4$ ) could potentially be attributed to the presence of the determinative IL@Ru(II).  $DFCoMn_2O_4$  exhibited an IV isotherm and a ring hysteresis of H1-type, signifying the entity of mesoporous structures (refer to Fig. 6). The magnitude of the vents was determined by utilizing the desorption portion of the nitrogen isotherm through the application of the BJH method. The results from these calculations indicated that the dimensions of these vents were approximately



Scheme 1. Co-immobilization procedure of IL@Ru(II) onto  $DFCoMn_2O_4$ .

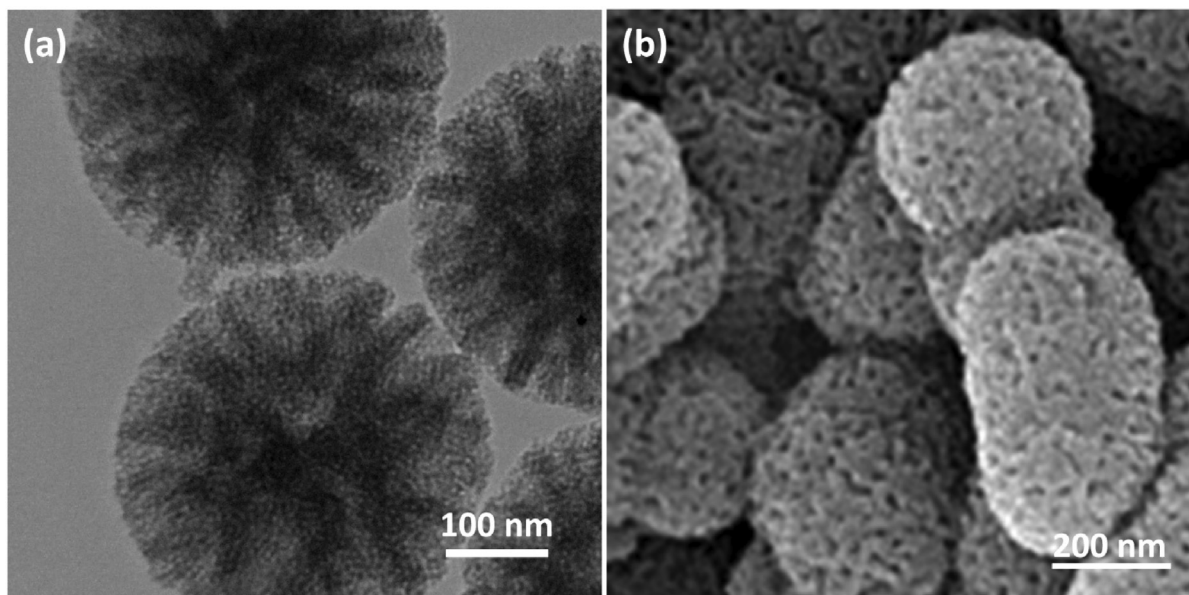


Fig. 1. TEM photos of  $DFCoMn_2O_4/IL@Ru(II)$  (a); FE-SEM photos of  $DFCoMn_2O_4/IL@Ru(II)$  (b).

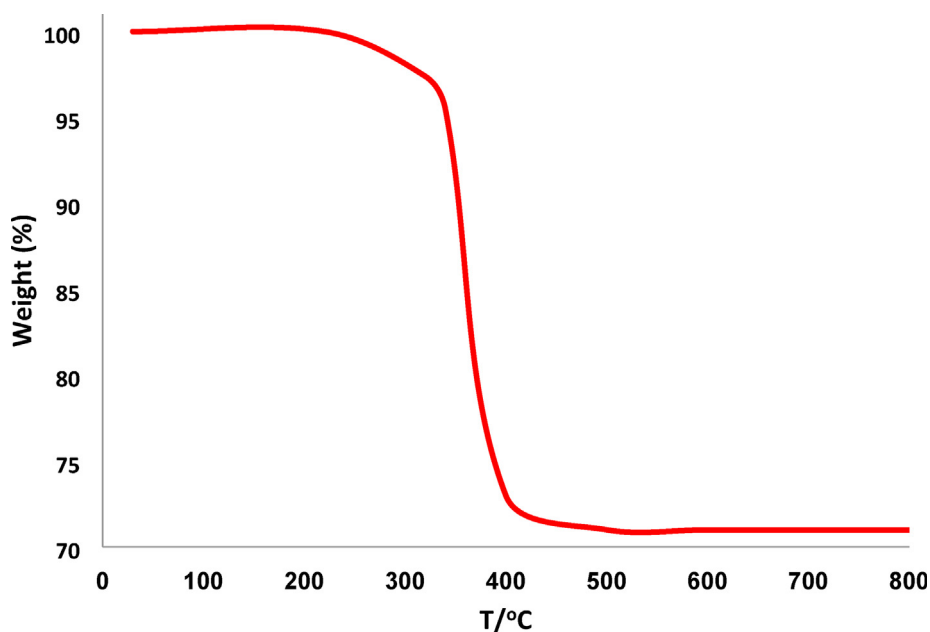


Fig. 2. TGA diagram of  $DFCoMn_2O_4/IL@Ru(II)$ .

13 nm (Table 1). The substantial quantity and capability of mesoporous  $DFCoMn_2O_4$  were able to accommodate  $IL@Ru(II)$  that possesses a vast molecular magnitude.

The Taguchi method is widely known in contemporary robust design methodologies, which are rooted in the principles of experimental design (Jiang et al., 2023). This specific methodology in engineering is employed in order to decrease vulnerability to factors that lead to deviation, improve the conditions of the process, and lower costs associated with development and production, thus yielding superior quality products. The Taguchi approach typically employs two key instruments, namely the signal-to-noise ratio ( $S/N$ ) for assessing induction quality and the orthogonal array for concurrently dealing with multiple design factors. The Taguchi experimental design encompasses four essential stages: (1) elucidating

the components and specifying the numerical values of factors, (2) selecting the orthogonal array based on the elements and their levels, (3) conducting tests to obtain data according to the specified orthogonal sequence, and (4) analyzing the data obtained from the analysis of variance of the signal-to-noise ratio (ANOVA). The initial crucial phase involves the meticulous selection of factors and their corresponding levels. The objective of this particular investigation was to identify the most noteworthy variables that contribute to the attainment of optimal reaction performance, all while operating within the limitations imposed by a restricted number of trials. In order to gauge the quantitative impact of asphaltene on reaction efficiency, four distinct levels (200, 1000, 2000, and 2500 mg/L) were deliberately selected for examination. Additionally, to assess the role of temperature in the reaction, four

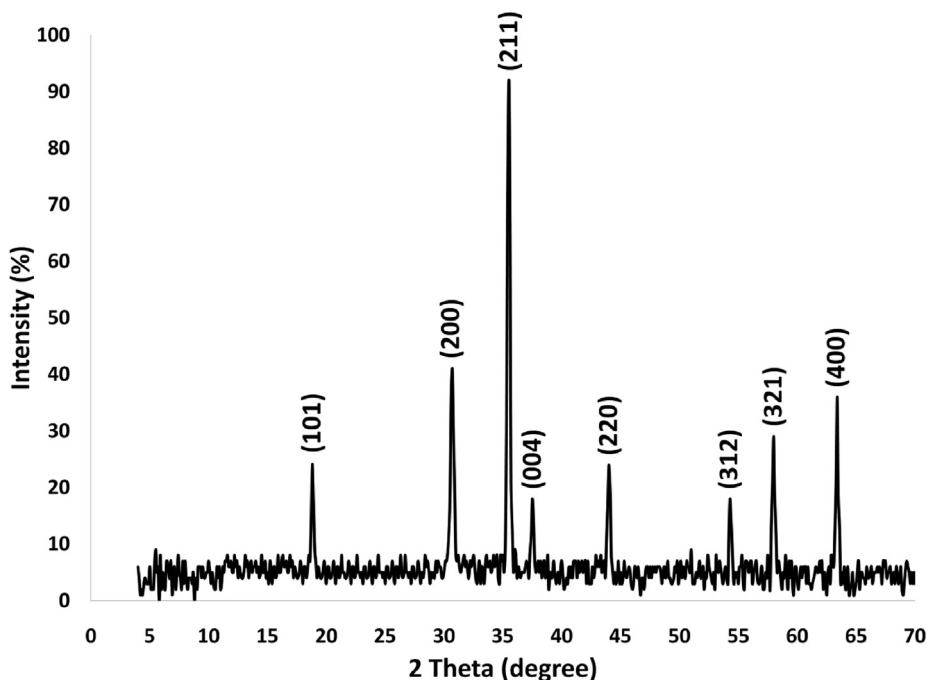


Fig. 3. XRD analysis of fibrous  $DFCoMn_2O_4/IL@Ru(II)$ .

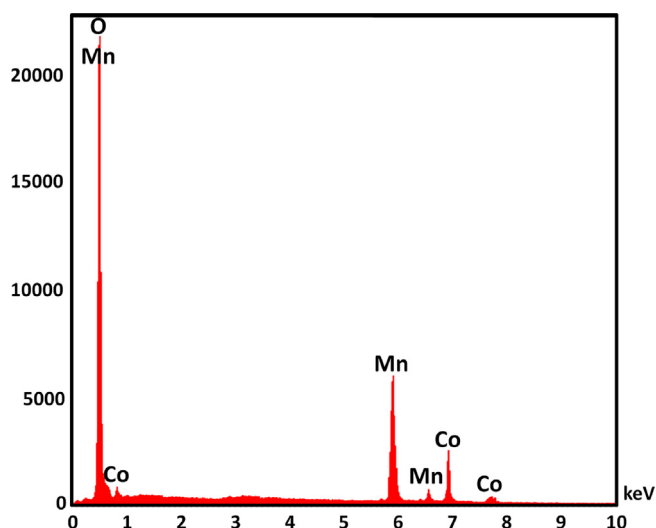


Fig. 4. EDX pattern of fabricated  $DFCoMn_2O_4$ .

varying temperatures (298, 302, 308, and 314 K) were chosen for investigation. Eventually, the quantities of adsorbent were selected at 0.3, 0.5, 0.7, and 1.0 g/L to investigate their impact. Consequently, a Taguchi experiment was designed with three parameters, each having four levels (Table 2). The selection of these parameter levels was based on prior screening experiments and existing literature (Chen et al., 2023). In order to carry out this experimental design, a standard L16 orthogonal array was employed (Table 3).

Each entry within Table 4 represents an individual scientific investigation conducted within specific conditions. The selection of maximal responses was made in order to optimize the efficiency of reactions. Consequently, a formula with a “bigger-the-better” characteristic was employed to determine the combination of parameters that yielded the highest efficiencies, as outlined below:

$$\frac{S}{N} = -10 \log \left( \frac{1}{n} \sum_{i=1}^n \frac{1}{y_i^2} \right)$$

Where the signal-to-ratio (S/N) is based on improving quality and price by reducing variability,  $n$  represents the number of specimens per experiment, and  $y$  is the efficiency. In this particular investigation, each experiment was conducted three times ( $n = 3$ ) under similar conditions in order to assess the impact of noise. The Minitab software was utilized to analyze the outcomes, and ANOVA was employed to determine the influence of each parameter on the yield within the framework of the Taguchi approach. In order to conduct an analysis, careful consideration was given to the efficiency of reactions. The ANOVA table provides a comprehensive overview of the various parameters' impacts on the yield, as illustrated in Table 5. Significantly, the amount of adsorbent emerged as the dominant factor, accounting for 38.34% of the overall influence. In comparison, the asphaltene quantity and temperature made contributions of 27.18% and 32.81% respectively. It is worth noting that this error did not have a substantial impact on the yield, thereby demonstrating the efficacy of the selected parameters in enhancing the overall output.

The Taguchi methodology delineates the optimal conditions under which uncontrollable variables, commonly referred to as noise, exert the least impact on the output of a system. In the Taguchi approach, the signal-to-noise ratio (S/N) serves as a metric to elucidate the respective contributions of different factors towards variations. The graphical representation in Fig. 6a illustrates the role of each level of asphaltene adsorption on the yield of the reaction. It is apparent that the final level exhibits the highest value for the S/N ratio, amounting to 39.24. Hence, it exerted the most significant impact on the production output when compared to the other degrees of this given characteristic. The outcome is depicted in Fig. 6b, which showcases the effect of distinct temperatures on the yield. In accordance with Fig. 6a, it is evident that the temperature of 298 K achieved the highest signal-to-noise ratio (S/N). The rise in temperature resulted in enhanced mobility of molecules and consequently facilitates accessibility to the active centers of the reaction. This phenomenon positively affects the overall perfor-

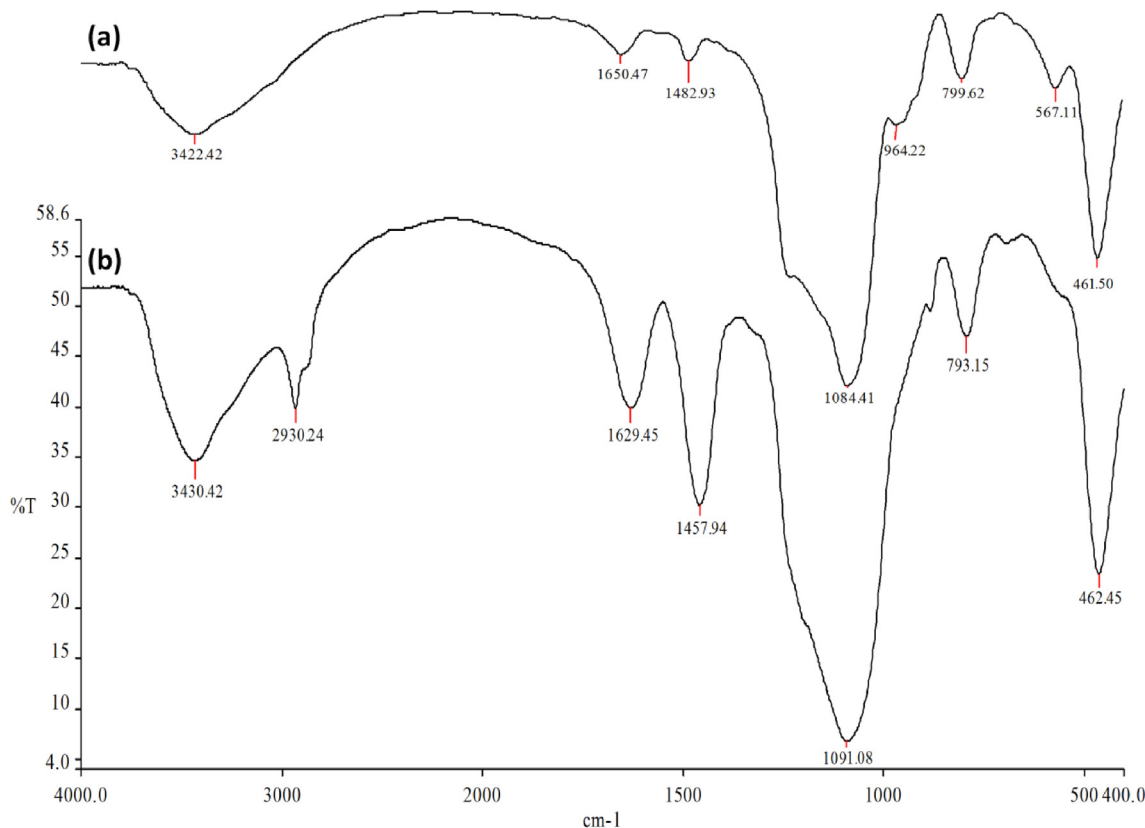


Fig. 5. FTIR spectra of DFCoMn<sub>2</sub>O<sub>4</sub> (a), and DFCoMn<sub>2</sub>O<sub>4</sub>/IL@Ru(II) (b).

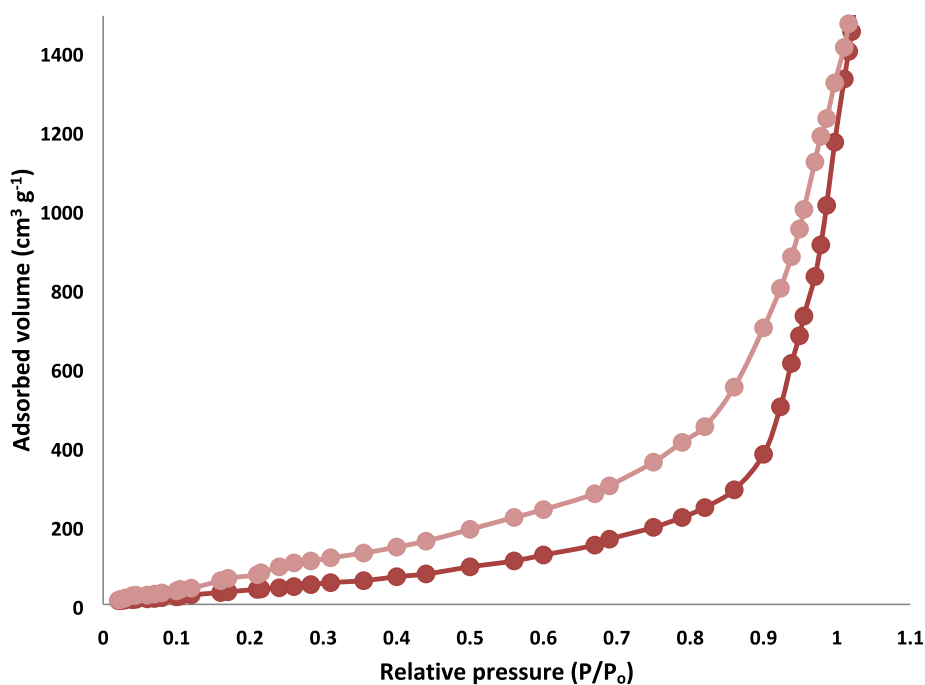


Fig. 6. Adsorption-desorption isotherms of DFCoMn<sub>2</sub>O<sub>4</sub>/IL@Ru(II).

mance. However, when the temperature surpasses the optimal threshold, the yield diminishes due to the detrimental effect on the active centers. According to the data provided in Fig. 6c, it can be observed that the third level of the adsorbent value param-

eter exhibited the highest signal-to-noise value. Consequently, this particular level exerted the most notable role in the yield of the adsorbent value when compared to the other levels. Upon reaching the optimal value of the adsorbent, the active centers experienced

**Table 1**  
Anatomical elements of  $DFCoMn_2O_4$ , and  $DFCoMn_2O_4/IL@Ru(II)$ .

Nanoadsorbents	$S_{BET}$ ( $m^2/g$ )	$V_a$ ( $cm^3 g^{-1}$ )	$D_{BJH}$ (nm)
$DFCoMn_2O_4$	709	2.9	15
$DFCoMn_2O_4/IL@Ru(II)$	386	2.1	10

**Table 2**  
Parameters and their corresponding level values.

Factors	Level 1 (A)	Level 2 (B)	Level 3 (C)	Level 4 (D)
Asphaltene quantity	200 mg/L	1000 mg/L	2000 mg/L	2500 mg/L
Temperature (K)	298 K	302 K	308 K	314 K
Adsorbent amount (g/L)	0.3 g/L	0.5 g/L	0.7 g/L	1.0 g/L

**Table 3**  
Experimental design utilizing the L16 orthogonal array.

Run	A	B	C	D
1	1	1	1	1
2	1	2	2	2
3	1	3	2	3
4	1	4	4	3
5	2	2	3	2
6	2	1	2	3
7	2	3	1	4
8	3	4	3	2
9	2	3	4	3
10	3	4	4	2
11	3	3	2	1
12	4	3	1	2
13	4	2	4	3
14	4	1	3	2
15	2	3	4	4

an increase, resulting in a heightened rate and efficiency of the reaction. Subsequently, any increase in the adsorbent value beyond the optimal amount leads to a substantial augmentation in the number of active centers. This phenomenon can be attributed to the formation of various complexes, which in turn delays the production time.

In the optimization of various elements on the adsorption of asphaltene from petroleum, the quantity of  $DFCoMn_2O_4/IL@Ru(II)$  as a nanoadsorbent was examined first. The role of various quantities of  $DFCoMn_2O_4/IL@Ru(II)$  in the adsorption of asphaltene was probed. According to Fig. 7a, the highest adsorption ( $1.66 \text{ mg/m}^2$ ) took place in the existence of 0.5 g/L catalyst. To assess the impact

**Table 4**  
The efficiency of sample reactions.

Number of reaction	1	2	3	4	5	6	7	8	9	10	11	12	13	14	15
Efficiency (%)	61	82	71	64	75	78	74	91	88	93	90	77	72	87	80

**Table 5**  
Analysis of variance.

Source	DF	Seq SS	Adj SS	Adj MS	F	P	Contribution (%)
Asphaltene quantity	3	7.6947	7.6947	2.9147	26.14	0.014	38.34
Temperature	3	3.7122	3.7122	1.2069	13.04	0.043	27.18
Adsorbent amount	3	5.3416	5.3416	1.8364	18.29	0.028	32.81
Residual Error	3	0.2164	0.2164	0.0982	21.94	0.019	1.67
Total	12	16.9649					100

of primary quantity asphaltene, experiments with the quantity of 100 to 2500 mg/L asphaltene was done on  $DFCoMn_2O_4/IL@Ru(II)$  adsorbent in 3 h at 300 K. As can be seen in Fig. 7b, the primary quantity of asphaltene has a remarkable influence on the amount of its absorption rate. By raising asphaltene from 100 to 2500 mg/L, the quantity of asphaltene adsorption was enhanced. With the enhancement of asphaltene, the propulsive force of mass transfer rose and led to the enhancement of the adsorption capacity. In other words, enhancement of the primary quantity of adsorbent ameliorated its improved the adsorption rate and propulsion to transpire in the film layer. The results showed that the adsorbent can reach its maximum absorption capacity in the shortest time. The findings were in line with the past studies. Here, it was found that increasing the quantity of asphaltene at different temperatures increased absorption so that the adsorbent was saturated after 3 h (Fig. 7b). At r.t. of 100 mg/L, the experimental equilibrium adsorption  $q_e$  for the adsorbent was  $0.18 \text{ mg/m}^2$ , and it was improved to  $1.66 \text{ mg/m}^2$  when the quantity was enhanced to 2500 mg/L. This revealed that the nanoparticles were appropriate adsorbents for asphaltene. The findings revealed the robust adsorption capacity of  $DFCoMn_2O_4/IL@Ru(II)$ , which might be due to the existence of  $IL@Ru(II)$  categories immobilized on  $DFCoMn_2O_4$ . Strong adsorption by  $DFCoMn_2O_4/IL@Ru(II)$  adsorbent might be due to the synergistic influence of  $DFCoMn_2O_4$  and  $IL@Ru(II)$  adsorbent categories, which were great adsorbents of asphaltene. Furthermore, the existence of  $IL@Ru(II)$  categories in spherical anatomy and on  $DFCoMn_2O_4$  fibers led to the highest asphaltene adsorption.

Afterward, the quantity of asphaltene adsorbed in 2500 mg/L (optimal quantity) was investigated at 298, 302, 308, and 314 K. The optimal quantity of 0.5 g/L adsorbent was employed. Fig. 7c depicts the temperature effect in this reaction on  $DFCoMn_2O_4/IL@Ru(II)$  NPs. When the temperature rose to 314 K, the asphaltene adsorption capacity on the nanoadsorbent dropped. It was inferred that asphaltene absorption occurred more easily at a lower temperature. This was completely consistent with previous studies (Bohlooli Shaafi et al., 2021).

In addition, the influence of  $CoMn_2O_4/IL@Ru(II)$  NPs was compared with  $DFCoMn_2O_4/IL@Ru(II)$  NPs under ideal circumstances in the absence of fibrous structure of  $CoMn_2O_4$ . The experimental equilibrium adsorption  $q_e$  for the asphaltene adsorption of  $1.66 \text{ mg/m}^2$  specified that fibrous structure of  $CoMn_2O_4$  drastically enhanced the adsorption.  $IL@Ru(II)$  was responsible for catalyzing the conversion, and the heterogeneous features of  $DFCoMn_2O_4$  were deployed for proper separation of the adsorbent. The blank experiments in the non-attendance of any adsorbent revealed the only  $0.04 \text{ mg/m}^2$ . Considering the findings (Fig. 8),  $DFCoMn_2O_4/IL@Ru(II)$  was chosen as a more active adsorbent to boost other

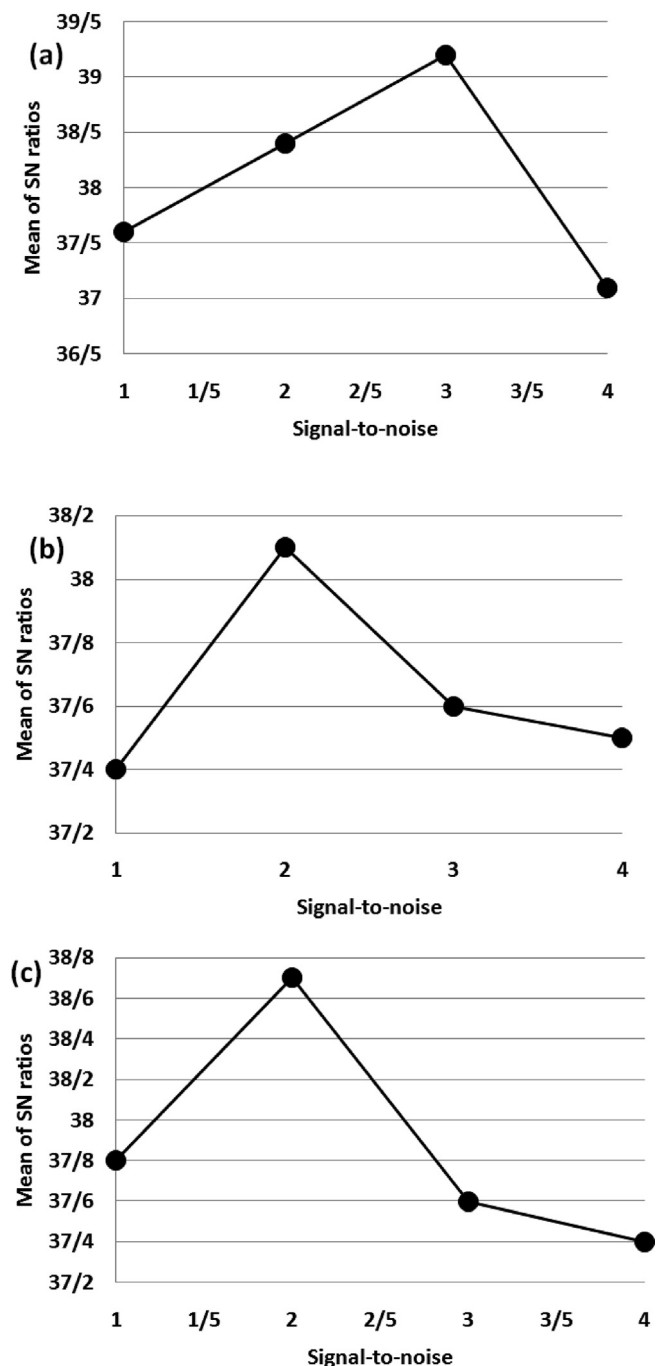


Fig. 7. Levels effect of parameters on reaction efficiency: Asphaltene quantity (a), temperature (b), and adsorbent amount (c).

parameters. This feature was due to the presence of IL on the nanoadsorbent. Maybe, the IL play the role of adsorbent in the asphaltene adsorption. Fig. 8 depicts the catalytic mechanisms involved in the oxidation of asphaltene using bimetallic nanocatalysts. The diagram illustrates the absorption of asphaltene by nanoparticles, primarily taking place at the active sites of  $DFCoMn_2O_4$ . Simultaneously, diatomic oxygen molecules are adsorbed onto the oxygen anion vacancies present on the support's surface. Consequently, a parallel redox cycle and asphaltene oxidation were observed in this process. Fig. 9.

For research the catalytic power of various  $DFCoMn_2O_4/IL@bi$ -pyridine metal complex as a nanoadsorbent, we examined their

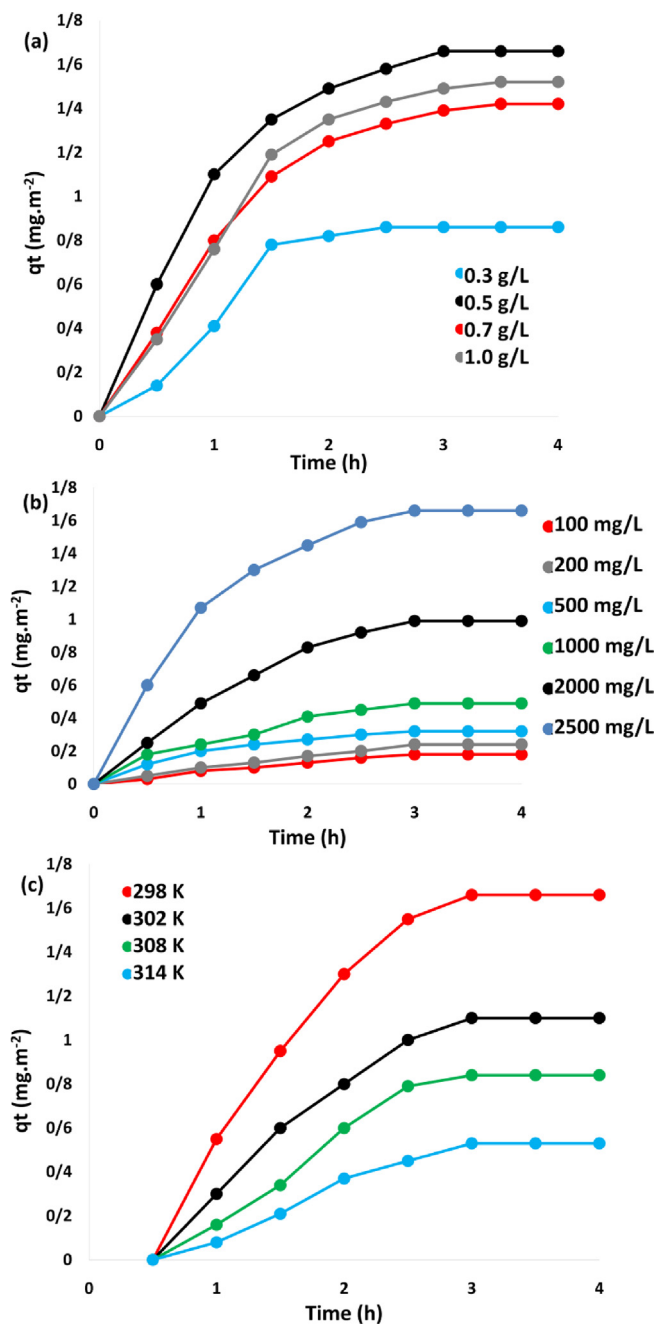


Fig. 8. Role of (a) catalyst amount; (b) asphaltene quantity; and (c) temperature on asphaltene adsorption.

efficiency on the asphaltene adsorption (Table 6). The catalytic activity of these nanoadsorbents were found to be of the order  $Ru(II) > Ni(II) > Cu(II) > Zn(II) > Cr(III) > Mn(II) > Cd(II) > Hg(II) > Co(II)$ . Therefore, we used complex of Ru, for the asphaltene adsorption.

The evaluation of asphaltene absorption by  $DFCoMn_2O_4/IL@Ru$  (II) enables the facilitation of their absorption kinetics prediction. The determination of the kinetic approach for asphaltene adsorption was carried out within a duration of 3 h, as durations exceeding this threshold may induce alterations in the adsorption process. Fitting of the data was conducted utilizing linear relationships in order to investigate the kinetics of the three models: Eq.1: intraparticle diffusion, Eq.2: quasi-second-order, and Eq.3: quasi-first-order. The equations of models are:

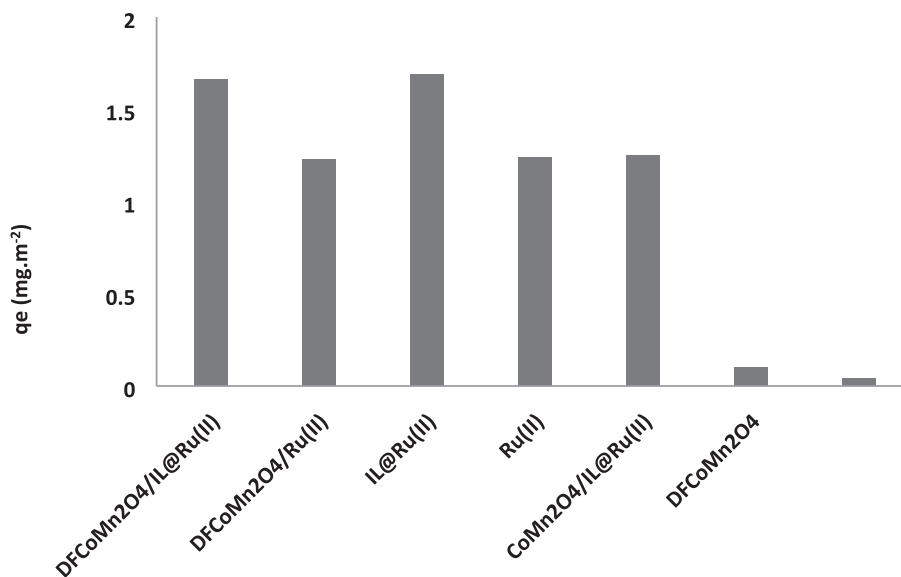


Fig. 9. Influence of adsorbent on the asphaltene adsorption.

Table 6

The effect of  $DFCoMn_2O_4/IL@bipyridine$  metal complex for the asphaltene adsorption.

Entry	Metal ion	$q_e$ ( $mg.m^{-2}$ )
1	Ru(III)	1.66
2	Cd(II)	0.47
3	Mn(II)	0.53
4	Cr(III)	0.94
5	Cu(II)	1.31
6	Hg(II)	0.41
7	Co(II)	0.33
8	Zn(II)	1.02
9	Ni(II)	1.34

<sup>a</sup>Isolated yield.

$$\text{Intraparticle diffusion : } q_t = k_1 t^{0.5} + 1 \quad (1)$$

$$\text{Quasi - second - order : } \frac{t}{q_t} = \frac{1}{k_2 q_e^2} + \frac{t}{q_e} \quad (2)$$

$$\text{Quasi - first - order : } \ln(q_e - q_t) = \ln(q_2) \quad (3)$$

To illustrate the strength and adsorption performance of  $DFCoMn_2O_4/IL@Ru(II)$  adsorbent, the adsorbent reusability was probed for 5 succeeding runs. To investigate the impact of  $DFCoMn_2O_4$  categories, the recovery capability of Ru(II) with  $DFCoMn_2O_4/IL@Ru(II)$  for asphaltene adsorption was studied in succeeding runs. After each reaction, the adsorbent was isolated,

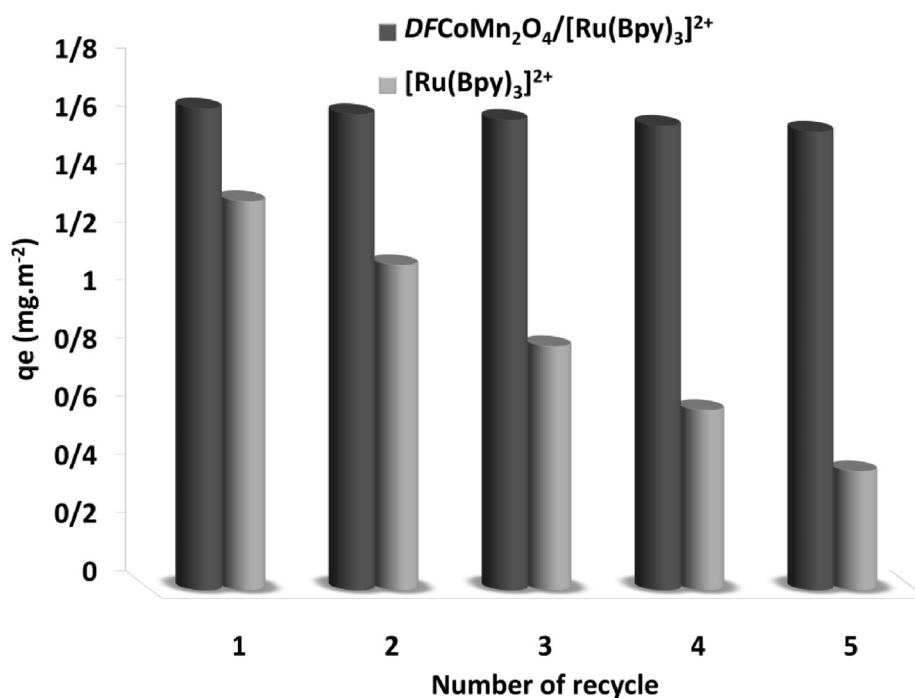


Fig. 10. Recoverability of  $DFCoMn_2O_4/IL@Ru(II)$  and  $IL@Ru(II)$  in asphaltene adsorption.

eluted with acid and water, and reutilized after warming up to 140 °C. Fig. 10 depicts the outcomes of the reusability examinations under ideal circumstances during 3 h. 0.5 g/L was utilized to assess the adsorption of Ru(II). Results were announced on the basis of  $q_e$  (in  $\text{mg}/\text{m}^2$ ). As Fig. 10 shows,  $\text{DFCoMn}_2\text{O}_4/\text{IL@Ru(II)}$  had a higher resistance to adsorption properties compared to Ru (II), and subsequently a negligible loss of activity during successive desorption/adsorption cycles. Asphaltene was observed. The  $q_e$  value of  $\text{DFCoMn}_2\text{O}_4/\text{IL@Ru(II)}$  NPs, changed from 1.66 to 1.58  $\text{mg}/\text{m}^2$  after 5 continuous desorption/adsorptions of asphaltene. However, this change for Ru(II) enhanced from 1.34 to 0.41  $\text{mg}/\text{m}^2$  during the continuous runs, which was notable in comparison with  $\text{DFCoMn}_2\text{O}_4/\text{IL@Ru(II)}$ .

To assess the variation in the adsorbent's composition, an initial hot filtration test was conducted, which demonstrated that the

adsorbent became separated after a duration of 1.5 h with a concentration of 1.35 ( $\text{mg}/\text{m}^2$ ). Subsequently, the product exhibited an effectiveness of 1.4 ( $\text{mg}/\text{m}^2$ ) after the aforementioned 1.5-hour interval. During the process of reaction, the heterogeneous nature of the  $\text{DFCoMn}_2\text{O}_4/\text{IL@Ru(II)}$  adsorbent was affirmed, with only a minor release observed. Furthermore, in order to validate the heterogeneity of the  $\text{DFCoMn}_2\text{O}_4/\text{IL@Ru(II)}$  adsorbent, the level of Mercury toxicity was measured. This analysis revealed that Mercury (0) had a profound deactivating effect on the metal adsorbent, thereby diminishing the activity of the nanoadsorbent. The investigations carried out in this study provided evidence for the heterogeneity of the adsorbent and the absence of metal leaching as a consequence of asphaltene adsorption (Fig. 11). The structure of the recovered  $\text{DFCoMn}_2\text{O}_4/\text{IL@Ru(II)}$  NPs was examined using XRD and TEM techniques in order to validate its stability

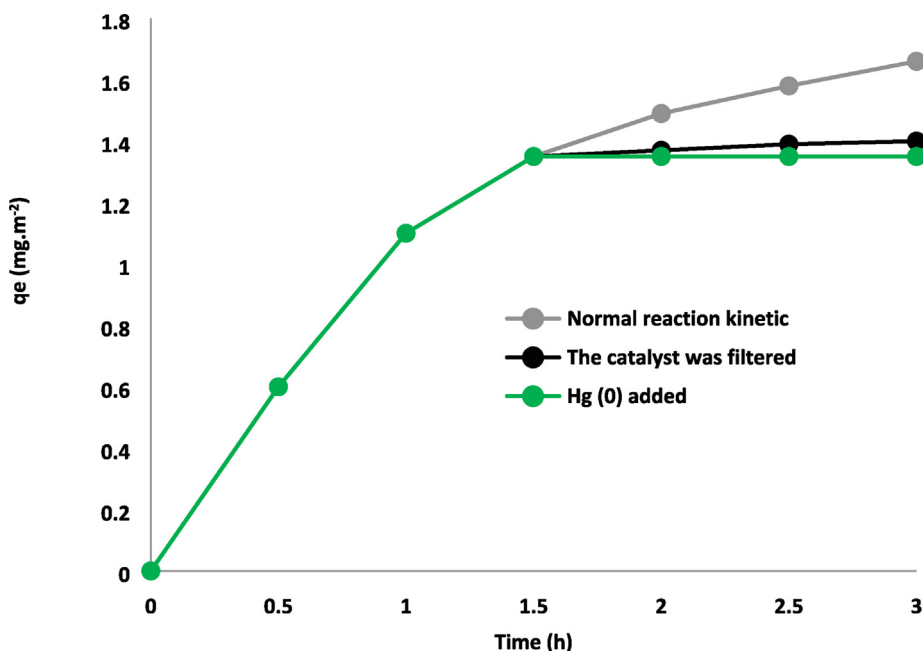


Fig. 11. Hot filtration, Reaction kinetics, and Hg (0) poisoning research for asphaltene adsorption.

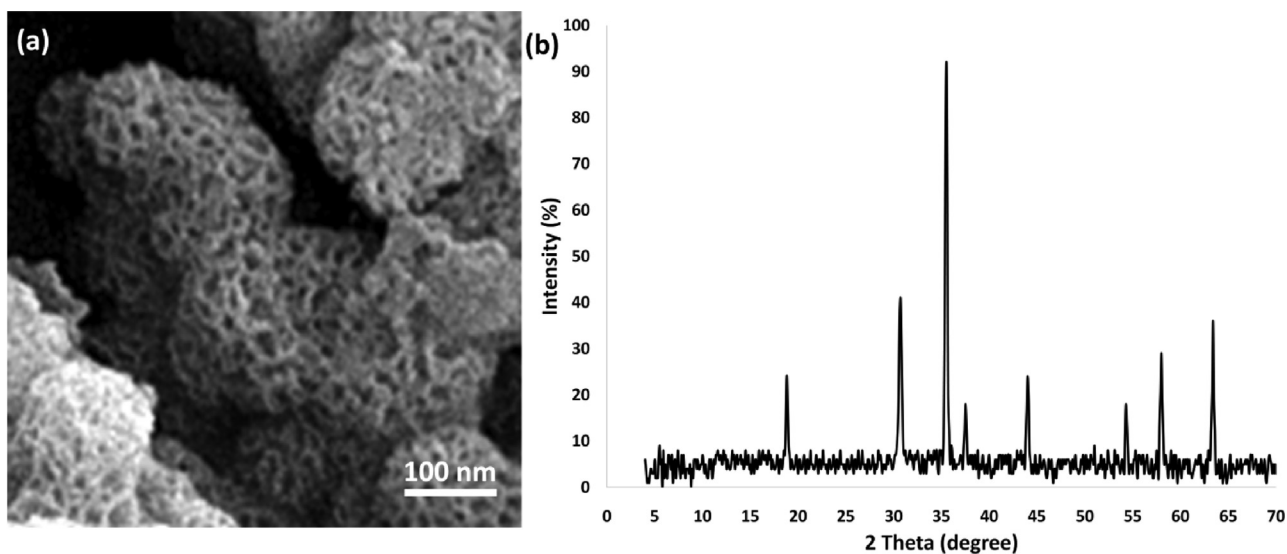


Fig. 12. (a) FE-SEM and (b) X-ray Diffraction (XRD) of the recovered  $\text{DFCoMn}_2\text{O}_4/\text{IL@Ru(II)}$  after ten times recovery for asphaltene adsorption.

(Fig. 12). Following the reuse of  $DFCoMn_2O_4/IL@Ru(II)$  NPs for six cycles, no alterations were detected in the XRD and TEM spectra prior to and after the reaction.

#### 4. Conclusion

A recoverable and effective adsorbent for the efficient adsorption/elimination of asphaltene was created from petroleum by immobilizing sulfated  $IL@Ru(II)$  on  $DFCoMn_2O_4$ . The anatomical traits and physical of the adsorbent were probed by XRD, TGA, FTIR, EDS, FE-SEM, BET, and TEM analyses. The best adsorption took place at room temperature, 2500 mg/ L of asphaltene, and the existence of 0.5 g/L nanoadsorbent. Asphaltene adsorption by nanoadsorbent followed quasi-second-order adsorption kinetics, illustrating the dependence of the procedure on the asphaltene amount. Another benefit of NPs was their ability to be reutilized after acid and heat treatment as an asphaltene adsorbent for succeeding cycles without a notable drop in function. The outcome highlighted the great stability of the adsorbent and the ability to preserve its adsorption trait.

#### Declaration of competing interest

The authors declare that they have no known competing financial interests or personal relationships that could have appeared to influence the work reported in this paper.

#### References

- Alalwani, T.A.A.M., Abdtawfeeq, T.H., Riadi, Y., Hadrawi, S.K., Chupradit, S., Danshina, S., 2023. *Inorg. Chem. Commun.* 148, 110222.
- Arias-Madrid, D., Medina, O.E., Gallego, J., Acevedo, S., Correa-Espinal, A.A., Cortés, F., Franco, C.A., 2020. *Catalysts* 10, 569.
- Bai, J., Li, X., Liu, G., Qian, Y., Xiong, S., 2014. *Adv. Funct. Mater.* 24, 3012–3020.
- Besikiotis, V., Knee, C.S., Ahmed, I., Haugsrud, R., Norby, T., 2012. *Solid State Ionics* 228, 1–7.
- Bezerra Lopes, F.W., de Souza, C.P., Vieira de Moraes, A.M., Dallas, J.P., Gavarrri, J.R., 2009. *Hydrometall.* 97, 167–172.
- Bohlooli Shaafi, F., Motavalizadehkakhky, A., Zhiani, R., Nourid, S.M.M., Hosseiny, M., 2021. *RSC Adv.* 11, 26174–26187.
- Cao, X., Vassen, R., Fischer, W., Tietz, F., Jungen, W., Stover, D., 2003. *Adv. Mater.* 15, 1438–1442.
- Chen, S., Li, J., Yang, L., Chen, J., Zhiani, R., 2023. *J. CO<sub>2</sub> Utiliz.* 72, 102509.
- Fujiwara, Y., Dixon, J.A., Rodriguez, R.A., Baxter, R.D., Dixon, D.D., Collins, M.R., Blackmond, D.G., Baran, P.S., 2016. *J. Am. Chem. Soc.* 138, 1494–1497.
- Hassankhani, A., Sadeghzadeh, S.M., Zhiani, R., 2018. *RSC Adv.* 8, 8761–8769.
- Holmberg, R.J., Hutchings, A.-J., Habib, F., Korobkov, I., Scaiano, J.C., Murugesu, M., 2013. *Inorg. Chem.* 52, 14411–14418.
- Huang, Y., Li, H., Wang, Z., Zhu, M., Pei, Z., Xue, Q., Huang, Y., Zhi, C., 2016. *Nano Energy* 22, 422–438.
- Jiang, S.J., Chu, S.C., Zou, F.M., Shan, J., Zheng, S.G., Pan, J.S., 2023. *Math. Comput. Simul.* 203, 306–327.
- Khan, F.-A., Süß-Fink, G., 2012. *Eur. J. Inorg. Chem.* 2012, 727–732.
- Liu, C., Li, F., Ma, L.P., Cheng, H.M., 2010. *Adv. Mater.* 22, E28–E62.
- Liu, Z.G., Ouyang, J.H., Sun, K.N., 2011. *Fuel Cell.* 11, 153–157.
- Medina, O.E., Caro-Vélez, C., Gallego, J., Cortés, F.B., Lopera, S.H., Franco, C.A., 2019. *Nanomaterials* 9, 1755.
- Medina, O.E., Gallego, J., Olmos, C.M., Chen, X., Cortés, F.B., Franco, C.A., 2020. *Energy Fuels* 34, 6261–6278.
- Medina, O.E., Gallego, J., Pérez-Cadenas, A.F., Carrasco-Marín, F., Cortés, F.B., Franco, C.A., 2021. *Energy Fuels* 35, 18170–18184.
- Medina, O.E., Gallego, J., Acevedo, S., Riazzi, M., Ocampo-Pérez, R., Cortés, F.B., Franco, C.A., 2021. *Nanomaterials* 11, 1301.
- Medina, O.E., Moncayo-Riascos, I., Franco, C.A., Cortés, F.B., *Appl. A.C.S.*, 2023. *Nano Mater.* 6, 12805–12815.
- Meng, G., Ma, G., Ma, Q., Peng, R., Liu, X., 2007. *Solid State Ion.* 178, 697–703.
- Pikul, J.H., Gang Zhang, H., Cho, J., Braun, P.V., King, W.P., 2013. *Nat. Commun.* 4, 1732.
- Rosado Piquer, L., Jiménez Romero, E., Lan, Y., Wernsdorfer, W., Aromí, G., Sañudo, E. C., 2017. *Inorg. Chem. Front.* 4, 595–603.
- Sadeghzadeh, S.M., 2016. *Res. Chem. Intermed.* 42, 2317–2328.
- Salehi, Z., Zinatloo-Ajabshir, S., Salavati-Niasari, M., 2016. *J. Mol. Liq.* 222, 218–224.
- Salehi, Z., Zinatloo-Ajabshir, S., Salavati-Niasari, M., 2016. *RSC Adv.* 6, 26895–26901.
- Sanchez-Bautista, C., Dos santos-García, A.J., Pena-Martínez, J., Canales-Vázquez, J., 2010. *Solid State Ion.* 181, 1665–1673.
- Steele, B.C.H., Heinzl, A., 2001. *Nature* 414, 345–352.
- Wang, C., Huang, W., Wang, Y., Cheng, Y., Zou, B., Fan, X., Yang, J., Cao, X., 2012. *Int. J. Refract. Metals Hard Mater.* 31, 242–246.
- Wang, X., Ma, H., Wang, D., Wang, L., Yang, Y., Han, J., Qu, W., Yang, L., Wang, S., Tian, Z., 2023. *ACS Omega* 8 (18), 16384–16394.
- Wang, C., Wang, Y., Zhang, A., Cheng, Y., Chi, F., Yu, Z., 2013. *J. Mater. Sci.* 48, 8133–8139.
- Wu, L., He, Y.-M., Fan, Q.-H., 2011. *Adv. Synth. Catal.* 353, 2915–2919.
- Yang, J., Zhang, F., Wang, X., He, D., Wu, G., Yang, Q., Hong, X., Wu, Y., Li, Y., 2016. *Angew. Chem. Int. Ed.* 55, 12854–12858.
- Yao, Y., He, D.S., Lin, Y., Feng, X., Wang, X., Yin, P., Hong, X., Zhou, G., Wu, Y., Li, Y., 2016. *Angew. Chem. Int. Ed.* 55, 5501–5505.
- Zhao, Z., Yang, H., He, J., Hu, F., Cheng, F., Liu, H., Gong, C., Wen, S., 2023. *Molecules* 28, 5362.
- Zhiani, R., Saadati, S.M., Zahedifar, M., Sadeghzadeh, S.M., 2018. *Catal. Lett.* 148, 2487–2500.
- Zhu, S.J., Jia, J.Q., Wang, T., Zhao, D., Yang, J., Dong, F., Shang, Z.G., Zhang, Y.X., 2015. *Chem. Commun.* 51, 14840–14843.
- Zinatloo-Ajabshir, S., Salehi, Z., Salavati-Niasari, M., 2016. *RSC Adv.* 6, 107785–107792.